

50 nm thick AlN film-based piezoelectric cantilevers for gravimetric detection

This article has been downloaded from IOPscience. Please scroll down to see the full text article.

2011 J. Micromech. Microeng. 21 085023

(<http://iopscience.iop.org/0960-1317/21/8/085023>)

View [the table of contents for this issue](#), or go to the [journal homepage](#) for more

Download details:

IP Address: 131.215.220.166

The article was downloaded on 14/03/2013 at 23:42

Please note that [terms and conditions apply](#).

50 nm thick AlN film-based piezoelectric cantilevers for gravimetric detection

P Ivaldi¹, J Abergel¹, M H Matheny², L G Villanueva², R B Karabalin²,
M L Roukes², P Andreucci¹, S Hentz^{1,2} and E Defay¹

¹ CEA-LETI, MINATEC Campus, 17 Rue des Martyrs, 38054 Grenoble Cedex 9, France

² Kavli Nanoscience Institute, California Institute of Technology, Pasadena, CA 91125, USA

E-mail: sebastien.hentz@cea.fr

Received 13 December 2010, in final form 23 May 2011

Published 12 July 2011

Online at stacks.iop.org/JMM/21/085023

Abstract

Due to low power operation, intrinsic integrability and compatibility with CMOS processing, aluminum nitride (AlN) piezoelectric (PZE) microcantilevers are a very attractive paradigm for resonant gas sensing. In this paper, we theoretically investigate their ultimate limit of detection and enunciate design rules for performance optimization. The reduction of the AlN layer thickness is found to be critical. We further report the successful development and implementation in cantilever structures with a 50 nm thick active PZE AlN layer. Material characterizations demonstrate that the PZE e_{31} coefficient can remain as high as 0.8 C m^{-2} . Electrically transduced frequency responses of the fabricated devices are in good agreement with analytical predictions. Finally, we demonstrate the excellent frequency stability with a 10^{-8} minimum Allan deviation. This exceptionally low noise operation allows us to expect a limit of detection as low as $53 \text{ zg } \mu\text{m}^{-2}$ and demonstrate the strong potential of AlN PZE microcantilevers for high resolution gas detection.

(Some figures in this article are in colour only in the electronic version)

1. Introduction

In the past few decades, micro-/nanoelectromechanical systems (M/NEMS) have extensively been used for resonant sensing. Mechanically resonant sensors rely on the change in frequency (from a change in inertial mass and/or stiffness), which can be used to detect the variations of the effective mass while particles are accreted on the surface of the device (mass sensing) [1], or of the variations of the applied loads on the device (force sensing) such as acceleration [2]. For mass sensors, the mass sensitivity, i.e. the amount of frequency variation for a given increase of mass, is given by the ratio $\frac{f_0}{M_{\text{eff}}}$ where M_{eff} is the effective mass and f_0 the unloaded resonance frequency. This is why, along with the recent progress in modern nano-fabrication tools, miniaturized devices with higher frequencies and lower masses have enabled the demonstration of important milestones such as atomic scale resolution [3, 4].

One important application for the M/NEMS resonant mass sensor is the detection of small concentrations of analyte molecules in a gaseous solution [5]. In this case, the

mechanical structure is covered with a chemically active layer which preferentially adsorbs the targeted analyte. The accreted mass is thus proportional to the resonator surface. This gives a tradeoff between mass sensitivity and capture area. Due to this trade off, 'bigger' micromechanical resonators such as FBARs [6], SAWs [7], CMUTs [8], contour mode resonators [9], and flexural beam resonators [5, 10] are still considered as valid gas sensing devices. However, flexural resonators offer the highest mass sensitivity per surface area [11] and cantilevers in particular offer a larger dynamic range [12], critical to detect extremely low analyte concentrations.

To date, several transduction techniques have been implemented to actuate and detect flexural motion of microcantilevers, namely electrostatic/capacitive [13], magnetostatic/magnetomotive [14], thermoelastic/piezoresistive [15, 16], optical [17] and piezoelectric (PZE) [9]. The latter is particularly advantageous as it requires neither strong dc biasing nor small gaps like electrostatic/capacitive transduction or external setups like magnetostatic/magnetomotive and optical transduction and consumes less power than thermoelastic/piezoresistive

transduction [18]. Additionally, the piezoelectricity is a stress-induced effect, as opposed to capacitive displacement transduction; hence, its transduction gain is unchanged when scaling the size down.

A relatively restricted number of PZE materials are available in thin film technology such as PZT [19], ZnO [20], AlN [21] and LiNO₃ [22]. Among them, AlN has recently encountered commercial success with FBAR and SAW resonators. AlN's particularly interesting features are high PZE coupling, low dielectric loss, good mechanical, chemical and thermal stability and most importantly compatibility with CMOS processing [23].

The use of ultrathin AlN PZE layer is particularly advantageous for the transduction of PZE flexural beam resonators. It maximizes the magnitude of the electric field at constant applied electric potential optimizing thus the actuation efficiency. More importantly, from the sensing point of view, it allows one to locate the active PZE layer as close as possible from the upper fiber of the beam, where stress and strain are concentrated, maximizing thus the piezoelectrically induced charges. On the other hand, existing AlN thin film deposition techniques are very limited and the fabrication of sub-100 nm AlN films with good PZE properties is still challenging today [24]. Recently, few tenths of micrometer long cantilevers with 100 nm thick active AlN layer have been demonstrated [25, 26]. These works concentrate only on the actuation and no data on the efficiency of the PZE detection with ultrathin AlN has been reported so far.

The main objective of this paper is to demonstrate the potential of 50 nm thick AlN film-based PZE microcantilevers for sensing applications. To this end, we first theoretically investigate their ultimate sensing performances and enunciate design rules. Then, we experimentally demonstrate the high sensing capabilities of those devices using structural, electrical and frequency stability characterization.

2. Gas sensing performance modeling and design optimization

2.1. Surface mass limit of detection

Let us first consider the general case of a flexural cantilever resonant gas sensor. In equilibrium conditions, the accreted mass δm can be related to the concentration c_g of the targeted analyte in the surrounding gas by [27]

$$\delta m = K t_{\text{chem}} S c_g \quad (1)$$

where K , t_{chem} and S are the partition coefficient of the couple analyte/chemically active layer, thickness and resonator surface, respectively. If δm remains small compared to the effective device mass, the relative resonance frequency shift can be obtained by differentiation of the resonance frequency expression:

$$\left(\frac{\delta f}{f_0}\right) = -\frac{1}{2} \frac{\delta m}{\mu S}. \quad (2)$$

Here μ , δf and f_0 are the surface mass density of the resonator (mass per unit length and width), the induced

frequency shift and the resonance frequency of the considered mode for sensing operation. Combining (1) and (2) leads to

$$c_g = \frac{2\mu}{K t_{\text{chem}}} \left(\frac{\delta f}{f_0}\right). \quad (3)$$

A choice of analyte/functionalization layer, setting the chemical transduction efficiency (i.e. $K t_{\text{chem}}$), is outside the scope of this paper. As we focus only on the geometrical design optimization, we can exclude these terms to concentrate on the so-called surface mass limit of detection (SMLOD) expressed in kg m^{-2} which is related to the minimum measurable relative frequency shift $\left(\frac{\delta f}{f_0}\right)_{\text{min}}$ by

$$\delta m_{\text{surf}} = 2\mu \left(\frac{\delta f}{f_0}\right)_{\text{min}}. \quad (4)$$

$\left(\frac{\delta f}{f_0}\right)_{\text{min}}$ can be evaluated as the RMS value of the relative frequency noise in the whole frequency measurement loop. Assuming only additive and stationary noise processes as well as linear elements, this latter quantity can be further related to the amplitude noise through the Robins formula [28, 29]

$$\left(\frac{\delta f}{f_0}\right)_{\text{min}} = \frac{\langle V_{\text{noise}} \rangle}{2Q \langle V_{\text{out}} \rangle} \quad (5)$$

where $\langle V_{\text{noise}} \rangle$, V_{out} and Q are the RMS values of the amplitude noise and signal amplitude at the output of the resonator and its quality factor. As a consequence the SMLOD can be written as

$$\delta m_{\text{surf}} = \frac{\mu \langle V_{\text{noise}} \rangle}{Q V_{\text{out}}}. \quad (6)$$

Based on this latter equation, high resolution cantilever-based gas sensor should then display a high quality factor, low surface mass and high signal to noise ratio (i.e. dynamic range).

2.2. Electromechanical modeling

PZE transduction of flexural motion requires the use of a multilayered stack. Figure 1 presents one possible implementation with a so-called elastic layer on top of which a PZE material layer, sandwiched between two metallic electrodes, is deposited. When a voltage difference is applied to the electrodes, the longitudinal strain of the PZE layer (inverse PZE effect) creates a bending moment due to the offset of the PZE layer with respect to the neutral axis of the cantilever. Conversely, when the cantilever is bent, the longitudinal stress in the PZE layer creates charges on the electrodes (direct PZE effect) leading to a so-called motional current. The electromechanical modeling of such heterogeneous multi-morph systems is largely reported in the literature [30–33]. Here, we only recall the derivation method and the useful results. Under the classical Euler–Bernoulli theory, the bending vibration equation can be written as

$$\mu W \frac{\partial^2 w}{\partial t^2} + \mu \Gamma \frac{\partial w}{\partial t} + \langle EI \rangle_{\text{eq}} \frac{\partial^4 w}{\partial x^4} = \frac{\partial^2 M_p}{\partial x^2}(x). \quad (7)$$

Here, W , Γ , and w are the width of the cantilever, the damping coefficient and the vertical displacement of the neutral plane, respectively. The neutral plane position at rest

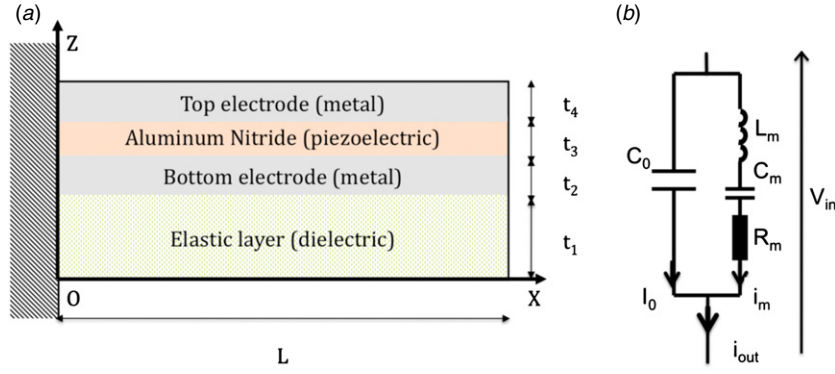


Figure 1. (a) Structure of a PZE heterogeneous multi-morph system incorporating an elastic layer on top of which a metal/PZE layer/metal stack is deposited. (b) Butterworth–Von Dyke equivalent circuit of the PZE bimorph; the metal/insulator/metal capacitance C_0 is responsible for the presence of a background current i_0 ; L_m , C_m , R_m represent the motional components arising from the mechanical resonance and are responsible for the presence of a so-called motional current i_m .

z_0 , and the equivalent beam rigidity $\langle EI \rangle_{eq}$, can be expressed using the equivalent beam approach [34]

$$z_0 = \frac{\sum E_i t_i z_i}{\sum E_i t_i}; \quad \langle EI \rangle_{eq} = \sum E_i I_i \quad (8)$$

where E_i , t_i , z_i and I_i are the Young’s modulus, the thickness, the mid-plane position and the quadratic momentum (with respect to z_0) of the i th material layer, respectively. As M_p is constant over the length of the beam, the driving term in equation (7) is zero except at the boundaries. We will then use the Heaviside function H to express the PZE momentum

$$M_p(x) = \left(\iint_{AIN} (z - z_0) e_{31} \frac{V_{in}}{t_3} dy dz \right) H(L - x) \quad (9)$$

$$= W \beta_p V_{in} H(L - x) \quad (10)$$

where V_{in} and e_{31} are the input actuation voltage and the effective transverse PZE coefficient, respectively. $\beta_p = e_{31}(t_3/2 + t_2 + t_1 - z_0)$ depends on the multilayer stack asymmetry and is a figure of merit of the actuation gain. Assuming small dissipation, equation (7) can be solved using Galerkin’s method where the general solution is given by

$$w(x, t) = \sum_n \lambda_n(t) \Phi_n(x) \quad (11)$$

where Φ_n are the undamped eigenmodes [34] and λ_n are the temporal amplitudes. Substituting (11) in (7) and using the orthogonality of the Φ_n , we obtain

$$\lambda_n(\omega) = \frac{WL\beta_p(\Phi'_n(L))}{\langle EI \rangle_{eq} \alpha_n^4} \frac{V_{in}}{1 + j(\omega/Q\omega_n) - (\omega/\omega_n)^2} \quad (12)$$

where α_n , $\omega_n = \left(\frac{\alpha_n}{L}\right)^2 \sqrt{\frac{\langle EI \rangle_{eq}}{\mu}}$ and Q are, respectively, the mode constant ($\alpha_1 = 1.875$, $\alpha_2 = 4.694$, ...), the n th mode resonance frequency and the quality factor. Assuming a sine wave actuation voltage at a frequency close to the n th resonant frequency, the input voltage–output current relation can be derived from Gauss’ theorem over one electrode area:

$$i_{out} = \frac{j\omega}{t_3} \iiint_{AIN} \left(e_{31}(z - z_0) \frac{\partial^2 w}{\partial x^2} - \epsilon_{33} \frac{V_{in}}{t_3} \right) dx dy dz \quad (13)$$

$$= j\omega \left(\frac{\frac{W^2 L \beta_p^2 \gamma_n}{\langle EI \rangle_{eq}}}{1 + j \frac{\omega}{Q_n \omega_n} - \frac{\omega^2}{\omega_n^2}} - C_0 \right) V_{in} \quad (14)$$

where $\gamma_n = \frac{[\Phi'_n(L)]^2}{\alpha_n^4}$ is a constant which only depends on the considered mode shape, and $C_0 = \epsilon_{33} \frac{(WL + S_{pads})}{t_3}$ is the static capacitance arising from the metal/insulator/metal structure, taking into account the mechanically not active areas (S_{pads}). Equation (14) is interpreted in terms of Butterworth–Von Dyke (BVD) electrical equivalent circuit [32] where the cantilever is modeled as a capacitance C_0 in parallel with a resonant R_m , L_m , C_m motional branch (figure 1) with

$$C_m = \frac{W^2 L \gamma_n \beta_p^2}{\langle EI \rangle_{eq}}; \quad L_m = \frac{1}{C_m \omega_n^2}; \quad R_m = \frac{1}{C_m Q \omega_n}.$$

It is possible to get rid of the current flowing through C_0 via a balancing technique in order to reduce background saturation and facilitate the frequency measurement. Several electronic circuits can be considered [35, 36], theoretically providing the same output signal. However, in practice, the circuit depicted in figure 4(b) presents the simplest and yet efficient and robust method, avoiding time consuming tuning of variable component and gain. Assuming a perfect balance of the bridge and considering that $QC_m \ll C_0$, C_p , the input/output electromechanical transfer function can be written as

$$V_{out} = \left(\frac{C_m}{2C_0 + C_p} \right) \frac{V_{in}}{1 + j \frac{\omega}{Q\omega_0} - \left(\frac{\omega}{\omega_0}\right)^2}, \quad (15)$$

where C_p is the load capacitance accounting for all parasitics.

2.3. Noise modeling

At this point, only two white noise processes are assumed to be present in the resonance frequency measurement loop to set the limit of detection. The first one is the first amplifier stage input noise with a power spectral density (PSD) in the electrical domain S_{amp} . The second one is the white noise generated on the electrode due to the Brownian motion of the device and called thermomechanical noise. From equipartition theorem,

its PSD can be expressed in the force domain by $S_f = \frac{2\rho_s}{\pi Q} k_b T$ [14]. Referred at the input of the first amplification stage and in the voltage domain, the thermomechanical noise PSD presents a Lorentzian shape characteristic of the device. However, considering a small measurement bandwidth BW , it is possible to use its peak value as a first approximation:

$$S_{V,th}(\omega) = \frac{2k_b T Q}{\pi L \omega_n^3} \left(\frac{\beta_p \Phi'_n(L)}{C_p + 2C_0} \right)^2. \quad (16)$$

In practice, for cantilever lengths between 1 and 100 μm , the input amplifier noise is largely dominant. Indeed, the state-of-the-art low noise amplifiers provide a noise floor of the order of 0.9 nV $\text{Hz}^{-1/2}$ [37] while the previous formula gives thermomechanical noise PSD level between 0.1 and 10 fV $\text{Hz}^{-1/2}$. The SMLOD can finally be expressed as

$$\delta m_{\text{surf}} = \frac{\sqrt{S_{\text{amp}} BW}}{Q^2 V_{\text{in}}} \frac{\mu(2 + C_p/C_0)}{C_m/C_0}. \quad (17)$$

2.4. Design optimization

The term $\frac{\sqrt{S_{\text{amp}} BW}}{Q V_{\text{in}}}$ in the previous equation can be considered independent of the geometrical properties of the cantilever. Theoretically, the quality factor Q in air should be dominated by viscous damping and should scale like $W \left(\frac{L}{\lambda}\right)^2$ [38]. Also the optimum voltage V_{in} should be limited by the onset of mechanical nonlinearity, equal to $\frac{6.3L}{\sqrt{Q}}$ [12]. However, these theoretical formulas do not account for our experimental results: Q varies significantly from one cantilever to another and the maximum input voltage is found to be much lower than expected. As a detailed study of Q and $V_{\text{in,max}}$ is out of the scope of this paper, we thus exclude them from this design optimization and use their mean experimental values for numerical calculations (100 and 750 mV, respectively).

The second term in equation (17) can be further split into three parts.

- *Surface mass density* $\mu = \sum \rho_i t_i$ where ρ_i stands for the mass density of each layer. This term is minimized when the total thickness of the beam is minimized, and especially when the heavy metallic electrodes are chosen to be as thin as possible.
- *Load* $(2 + C_p/C_0)$. The parasitic capacitance C_p can be reduced by bringing the first amplifier stage as close as possible to the cantilever. This can be done, for example, by integrating the resonator and its electronic on the same chip taking advantage of the compatibility of AlN with CMOS processing [23]. When $\frac{C_p}{C_0} \gg 2$, i.e. when C_p or the mechanically not active part of C_0 dominates, the SMLOD is inversely proportional to the device surface. In the opposite case, the SMLOD is unchanged with the device surface. In other words, in the practical size ranges, longer and wider cantilevers provide better performances up to the limit allowed by the fabrication process considering the presence of residual stress and thus of non-desired static deflection of the beam.

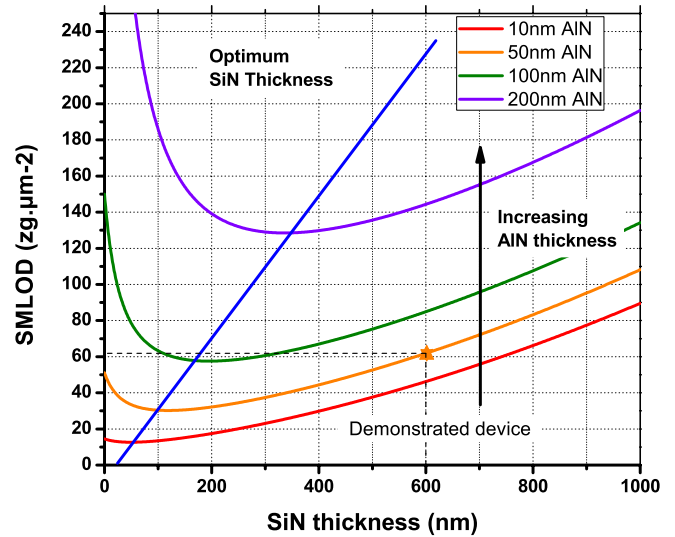


Figure 2. SMLOD as a function of the SiN layer thickness and for different AlN layer thicknesses. For comparison with experimental results, the bottom and top electrode thicknesses are equal to 100 nm and 25 nm, respectively, the parasitic capacitance is dominant and equal to 100 pF and the actuation voltage, quality factor, measurement bandwidth and the dominant noise are equal to 750 mV, 100, 0.1 Hz and 5 nV Hz^{-1} , respectively.

- *Motional capacitance over static capacitance ratio* C_m/C_0 . C_0 can be reduced by reducing the surface of the mechanically not active areas but at the cost of additional steps in the fabrication process. Ultimately, $C_0 = \epsilon_{33} \frac{WL}{t_s}$ and in this case C_m/C_0 depends only on the thicknesses of the different layers relative to each other. As illustrated in figure 2, for a given thickness of the AlN layer and of the electrodes, a tradeoff exists for the thickness of the elastic layer. Indeed, if it is too thin, β_p approaches zero and can be actuated only in plane motion, while if it is too thick the cantilever becomes too rigid to be deflected. Moreover, decreasing the AlN layer thicknesses drastically improves the transduction efficiency ratio $\frac{\beta_p^2}{\langle EI_{\text{eq}} \rangle}$ (see equation (14)). It increases the actuation electric field, decreases the equivalent rigidity $\langle EI_{\text{eq}} \rangle$ and puts the active AlN layer where the bending stress is maximum maximizing thus the piezoelectrically induced charges.

Within the dimension range where the product quality factor by the limit of nonlinearity does not scale, the general optimization strategy consists of increasing the length and the width while decreasing the thickness of the cantilever, as much as the fabrication process will allow. However, for a cantilever based on a material stack SiN/Pt/AlN/Pt and with a total thickness of $\sim 1 \mu\text{m}$, as used in the next section, more precise design rules can be enunciated as follows.

- The thickness of the AlN layer should be decreased as much as possible in order to improve the transduction efficiency (cf figure 2).
- The dense metallic electrodes should be chosen as thin as possible in order to minimize the mass density per unit length.

- The thickness of the SiN elastic layer should be chosen at its optimum value given by $\left. \frac{\partial C_m}{\partial t_1} \right|_{t_{2\min}; t_{3\min}; t_{4\min}} = 0$ (cf figure 2).
- The optimum length and width of the beam should be chosen to provide $C_0 > C_p$ and guarantee a negligible static deflection of the beam due to residual stress.

3. Experimental

3.1. Fabrication of 50 nm thick AlN films

As presented in the previous section, the key to improve the gas sensing performance of PZE microcantilevers is to decrease as much as possible the thickness of the PZE layer. The development of reliable AlN deposition techniques has been the focus of extensive research in the past decade [21, 24, 39–41]. Today, dc magnetron reactive sputtering is the most widely used technique and provides polycrystalline AlN films with PZE properties close to crystalline AlN [21]. According to [24], this deposition technique limits the reduction of the AlN layer thickness above 100 nm where AlN films present lower PZE properties and higher stress. Recent progress has however shown that further optimization can be carried out and is largely motivated by the demonstration of PZE NEMS [25, 26].

Starting from our well-stabilized AlN deposition process for bulk acoustic wave (BAW) resonators with usual thicknesses of 800 nm, we have investigated the material quality of 50 nm thick AlN films deposited on platinum (100 nm) electrodes on 200 mm silicon wafers. The residual stress is extracted from the wafer curvature (measured with a KLA-Tencor Flexus 2320) before and after the deposition of each layer with the help of the Stoney formula [21]. XRD patterns are acquired in both $\theta-2\theta$ and ω scans, respectively, for dominant orientation and rocking curve full width at half maximum (FWHM) quantification [21]. Finally the effective e_{31} transverse PZE coefficient is measured, thanks to the method reported in [42].

In agreement with the results reported in [24, 41], the residual stress can be modified from tensile to compressive by reducing the dc power, offering the opportunity to fabricate structures with a relatively low initial deflection. XRD measurements show that all fabricated films are fully c -axis oriented. The rocking curve FWHM is larger than its usual value for 800 nm thick films (2.4 versus 1.4) which does not necessarily degrade the PZE performances [25, 39, 40]: the effective e_{31} coefficient is actually found to be equal to 0.8 C m^{-2} , close to the state of the art [24] value.

3.2. Fabrication of microcantilevers

As presented in section 2.4, larger surface area cantilevers are expected to provide better performances. However, longer cantilevers are more sensitive to residual stress that causes initial bending or anchor failure. Thus, as opposed to [25, 26], where internal stress is controlled by optimizing AlN deposition parameters, several additional techniques had to be developed to overcome this difficulty. As a first step and to stay on the safe side, the SiN layer

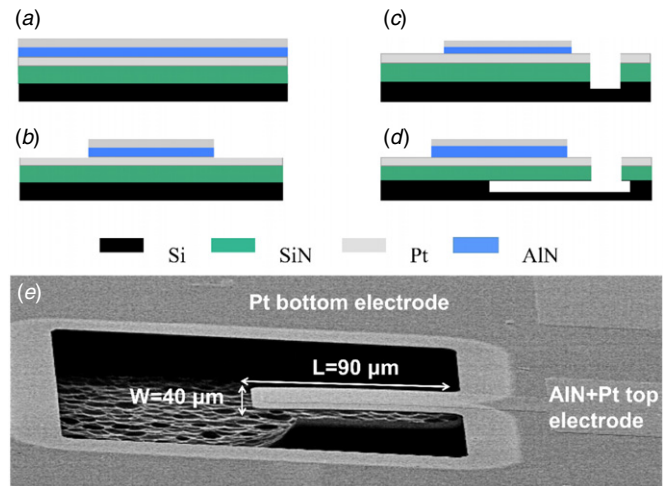


Figure 3. Fabrication process: (a) full sheet deposition of SiN (600 nm)/Pt (100 nm)/AlN (50 nm)/Pt (100 nm) stack on 200 mm Si wafers; (b) first lithographic step and ion beam etching (IBE) of the top Pt and AlN layers; (c) second lithographic step and subsequent IBE and reactive ion etching (RIE) of the bottom Pt and SiN elastic layer; (d) rapid thermal annealing (RTA) and XeF₂ isotropic etching of the Si substrate and (e) SEM picture of the fabricated cantilever.

thickness has been chosen greater than its optimal value (600 nm instead of a predicted 100 nm thickness, see figure 2), and then rapid thermal annealing has been performed prior to the release step in order to tune the top electrode stress and finally, the release depth has been kept minimum. Figure 3 presents the two lithographic step process used to fabricate our $90 \times 40 \mu\text{m}^2$ cantilever resonator (figure 3(e)). It starts with the full sheet deposition of SiN (600 nm)/Pt (100 nm)/AlN (50 nm)/Pt (25 nm) stack on 200 mm silicon wafers (figure 3(a)). The top platinum and AlN layers are then etched using ion beam etching (IBE), after the first lithography step (figure 3(b)). The bottom platinum and SiN layers are then patterned using subsequent IBE and reactive ion etching (RIE) after the second lithographic step (figure 3(c)). Finally, an isotropic XeF₂ etch of the silicon substrate is performed in order to release the cantilever structures (figure 3(d)).

3.3. Electrical characterization

For electrical characterization, a half-bridge circuit has been implemented with an unreleased cantilever as a dummy capacitor (figure 4). All measurements are performed in air with a SR844 lock-in amplifier. Figure 5 shows the frequency response of one of the tested cantilevers with four resonance peaks at 88 kHz, 546 kHz, 1.72 MHz and 3.46 MHz in good agreement with the analytical prediction given by $\omega_n = \left(\frac{\alpha_n}{L}\right)^2 \sqrt{\frac{EI_{\text{eq}}}{\mu}}$ for the flexural mode resonance frequency: 92 kHz, 578 kHz, 1.62 MHz and 3.17 MHz. This electrical scheme allows for the observation of several other peaks up to 20 MHz. It is also worth noticing that the quality factor of the four identified flexural modes increases while the maximum amplitude decreases. This decay is the result of the faster decrease of the electromechanical coupling ($\gamma_n \beta_p^2$) compared to the increase of Q .

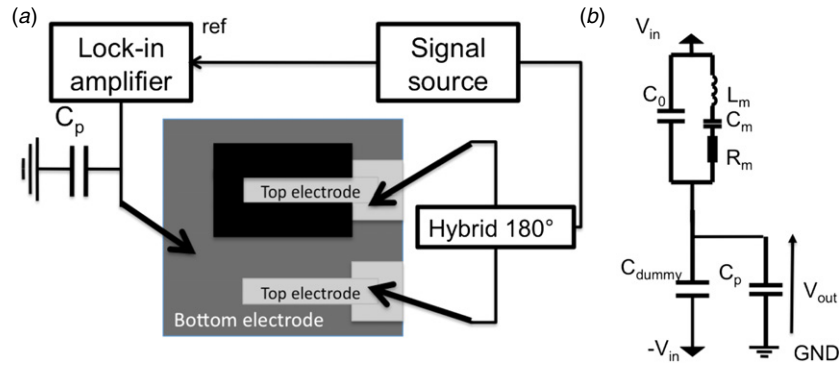


Figure 4. (a) On chip capacitive bridge used for frequency response characterization, an Agilent 33250A is used as a signal source to the on chip capacitive bridge and as a reference of the lock-in amplifier. The output signal is taken from the common bottom electrode and detected by the lock-in amplifier through the parasitic capacitance of connectors and cables. (b) Electrical equivalent network of the capacitive bridge using BVD representation of the PZE cantilever.

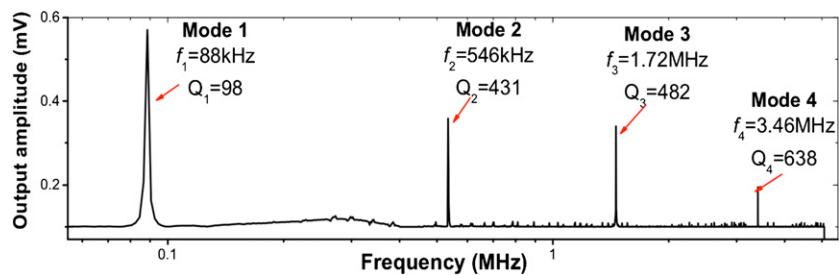


Figure 5. Frequency response of a 50 nm AlN film based PZE microcantilever resonator, the observed four resonance peaks correspond to the first four flexural modes of the cantilever. Theoretical resonance frequencies are 92 kHz, 578 kHz, 1.62 MHz and 3.17 MHz.

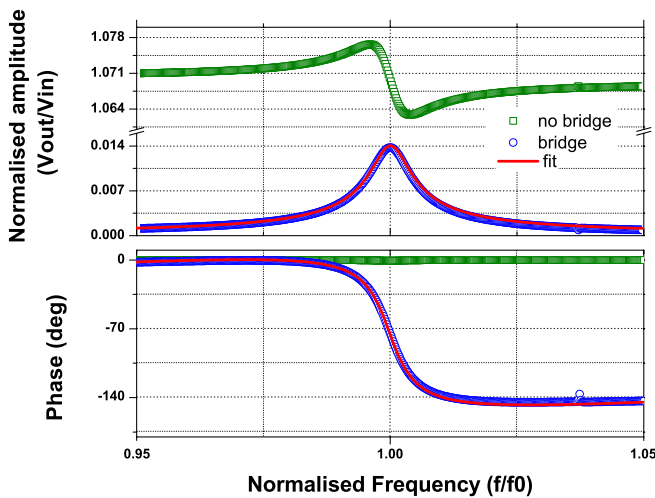


Figure 6. Electrical amplitude and phase of the first resonant mode of a 50 nm AlN film-based PZE microcantilever resonator, with and without capacitive bridge background compensation and fit with the analytical model developed in section 2.2. Note the almost undetectable phase jump in the case of no bridged.

Figure 6 illustrates the advantages of using the bridge architecture with a background signal reduced by two orders of magnitude. An $\sim 1\%$ mismatch in static capacitance between the cantilever and the dummy capacitor, observed on additional capacitance measurements, is responsible for the residual background. Taking it into account, analytical predictions provided by (15) can be fitted to experimental

results. For the cantilever used in figure 6, we obtain the numerical values of $Q = 125$ and $e_{31} = 0.78 \text{ C m}^{-2}$. This fitted effective e_{31} is very consistent with material measurements (see the previous section). However, the quality factor is very different from the one obtained with the cantilever of figures 4 but is still consistent with our assumption of an average value of 100. Finally, the maximum actuation voltage has been found to be equal to 750 mV above which stiffening nonlinearity occurs (figure 7). Using our analytical model, this input voltage corresponds to a displacement amplitude of 110 nm which is well below the theoretical limit of the mechanically induced nonlinearity [12].

3.4. Gas sensing performance assessment

Experimentally, the minimum measurable frequency shift is characterized by time domain resonance frequency variances such as the Allan deviation [43]. This estimator of the true variance is defined as one-half of the time average over N successive samples of the square of the differences between successive readings (with no dead time) of the mean relative frequency variation \bar{y}_k sampled over the sampling period τ and converges towards the RMS value of the frequency noise:

$$\sigma_{\text{Allan}}^2(\tau) = \frac{1}{N-1} \sum_1^N (\bar{y}_{k+1} - \bar{y}_k)^2. \quad (18)$$

Allan deviation measurements are performed using a closed frequency loop (self-oscillation or phase locked loop

Table 1. Surface Mass Limit Of Detection (SMLOD) reported in the literature for FBAR, SAW, NEMS flexural cantilevers, CMUT and our fabricated PZE microcantilever.

Resonant device	f_0	$\left(\frac{\delta f}{f_0}\right)_{\min}$	Integration time	SMLOD ($zg \mu m^{-2}$)
FBAR [6]	1.1 GHz	3×10^{-7}	NA	10 000
SAW [7]	158 MHz	7×10^{-8}	NA	700
AlN contour mode resonator [46]	220 MHz	$9 \cdot 10^{-8}$	100 ms	481
NEMS flexural resonators [5]	10 MHz	1.5×10^{-7}	10 s	400
CMUT [8]	18 MHz	3.5×10^{-8}	80 ms	77
50 nm AlN PZE microcantilevers	92 kHz	10^{-8}	10 s	53

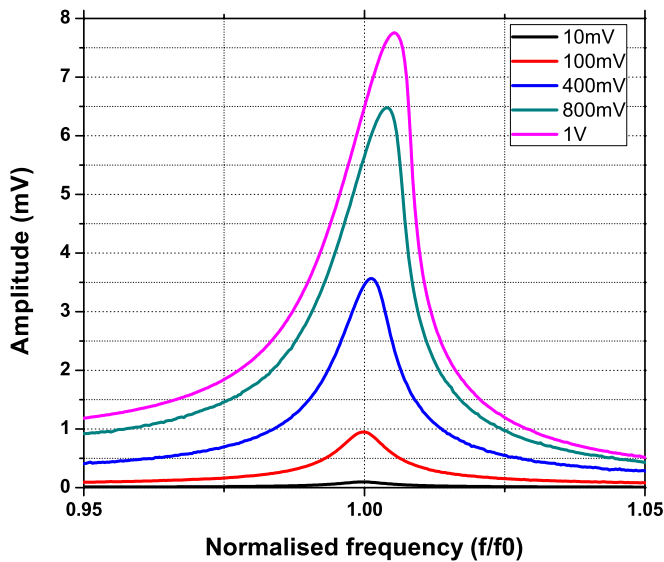


Figure 7. Electrical amplitude of the first resonant mode of a 50 nm AlN film-based PZE microcantilever resonator showing stiffening nonlinearity for actuation voltage higher than 800 mV.

circuit (PLL)). A real-time digital (MATLAB) PLL setup has been implemented by controlling the drive source frequency so as to maintain the phase (given by a lock-in amplifier) at 0, thanks to a custom corrector [44]. This scheme is limited by GPIB communication protocol and does not allow for the measurement of the Allan deviation at integration times shorter than roughly a few hundreds of ms. To access those, it is easier to use the circuit figure 4(a) in open loop and the method reported in [45]: the cantilever is driven at the first mode resonance frequency and the phase variations of the output signal are recorded. The Allan deviation is then computed from the measured phase noise assuming closed loop architecture with ideal feedback. For integration times between 1 s and 100 s, Allan deviation curves obtained with both methods are identical, which validate the open loop approach.

Figure 8 presents the results of Allan deviation measurements in an open loop for time constants between 10 ms and 100 s and input voltage between 50 mV and 750 mV. A satisfying agreement is also found with analytical estimation of the minimum measurable relative frequency shift. As expected from (6), the Allan deviation is proportional to the input voltage and scales like $\tau^{-1/2}$, which is consistent with the assumption of a dominant white additive noise. The minimum value of 10^{-8} obtained for the integration time of 10 s is

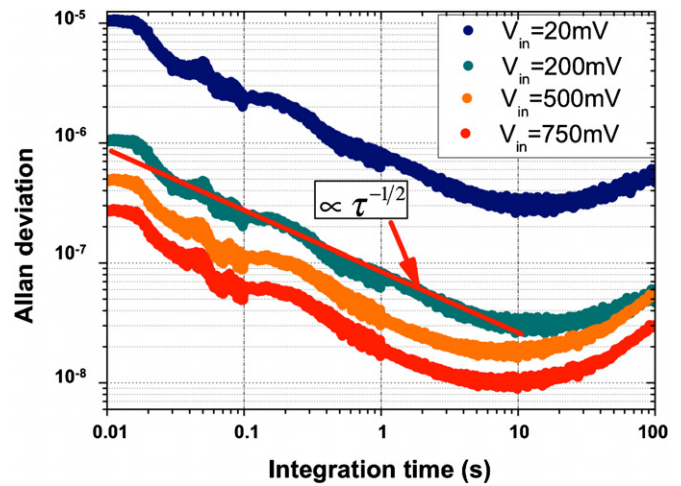


Figure 8. Allan deviation of a 50 nm thick AlN film-based PZE microcantilever for integration time between 10 ms and 100 s and input voltage between 50 mV and 750 mV (measured onset of nonlinearity).

also consistent with the manufacturer specifications giving the electronic noise of the lock-in amplifier ($5 \text{ nV Hz}^{-1/2}$).

Replacing in (4) the minimum measurable relative frequency shift by the minimum measured Allan deviation, and using available material data for the surface mass density μ , we obtain an expected SMLOD equal to $53 \text{ zg } \mu m^{-2}$ close to the value predicted in figure 2. Table 1 presents previously reported results of SMLOD and Allan deviation for different concurrent gravimetric sensor technologies. Although our fabricated cantilever does not exactly satisfy the design rules reported in section 2.5, our expected SMLOD is exceeded only by devices with relatively complex 1 GHz AlN resonators integrated on the same package with its CMOS detection circuit. Besides reducing the SiN thickness to its theoretical optimum value, further improvements of up to two orders of magnitude are expected by reducing both the parasitic capacitance and the noise, thanks to the integration of a low noise amplifier circuit as close as possible to the device itself.

4. Conclusion

Following theoretical and experimental approaches, we have demonstrated the tremendous potential of AlN PZE microcantilevers for gas sensing applications. Based on theoretical considerations, the key to performance optimization relies on the reduction of the AlN film thickness. We have thus optimized our deposition process and obtained 50 nm

thick AlN films with unprecedented PZE properties. Allan deviation measurements of a $90\ \mu\text{m} \times 40\ \mu\text{m} \times 885\ \text{nm}$ flexural micro-cantilever resonator embedding a 50 nm thick AlN film have shown a state-of-the-art SMLOD of $53\ \text{zg}\ \mu\text{m}^{-2}$, achieved with an actuation voltage lower than 1 V, with no dc polarization and a dissipated power on the order of a few nanowatts. This opens up new possibilities for portable low-power, extremely high resolution gas sensing applications. Future work will consist of fabricating and testing optimally designed devices, developing a functionalization chemistry, and showing the overall gas sensing capabilities with a few chosen analytes.

Acknowledgments

The fabrication of the experimental devices has been performed within the Plateforme des Technologie Amont (PTA) clean room. The authors also acknowledge the financial support of the Fulbright Doctoral Program and of the Carnot NEMS.

References

- [1] Li M, Tang H X and Roukes M L 2007 *Nat. Nanotechnol.* **2** 114–20
- [2] Seshia A A, Palaniapan M P, Roessig T A, Howe R T, Gooch R W, Schimert T R and Montagne S 2002 *IEEE/ASME J. MEMS* **11** 784–93
- [3] Yang Y T, Callegari C, Feng X L, Ekinci K L and Roukes M L 2006 *Nano Lett.* **6** 583–6
- [4] Jensen K, Kim K and Zettl A 2008 *Nat. Nanotechnol.* **3** 533–7
- [5] Li M, Myers E B, Tang H X, Aldridge S J, McCaig H C, Whiting J J, Simons R J, Lewis N S and Roukes M L 2010 *Nano Lett.* **10** 3899–903
- [6] Zhang H and Kim E 2005 *IEEE/ASME J. MEMS* **14** 699–706
- [7] Wang W, He S, Li S and Pan Y 2006 *Smart Mater. Struct.* **15** 1525–30
- [8] Lee H J, Park K K, Oralkan O, Kupnik M and Khuri-Yakub B T 2008 *IEEE Int. Freq. Control Symp. (Honolulu, HI)* vols 1 and 2 p 434–9
- [9] Piazza G, Stephanou P J and Pisano A P 2006 *IEEE/ASME J. MEMS* **15** 1406–18
- [10] Xu P, Li X, Yu H and Li J 2010 *J. Micromech. Microeng.* **20** 115003
- [11] Wenzel S W and White R M 1989 *Appl. Phys. Lett.* **54** 1976–8
- [12] Kacem N, Arcamone J, Perez-Murano F and Hentz S 2010 *J. Micromech. Microeng.* **20** 045023
- [13] Truitt P A, Hertzberg J B, Huang C C, Ekinci K L and Schwab K C 2007 *Nano Lett.* **7** 120–6
- [14] Ekinci K L, Huang M H and Roukes M L 2004 *Appl. Phys. Lett.* **84** 4469
- [15] Bargatin I, Kozinsky I and Roukes M L 2007 *Appl. Phys. Lett.* **90** 093116
- [16] Bargatin I, Myers E B, Arlett J, Gudelski B and Roukes M L 2005 *Appl. Phys. Lett.* **86** 133109
- [17] Kouh T, Karabacak D and Ekinci K L 2005 *Appl. Phys. Lett.* **86** 013106
- [18] Adams J D, Parrott G, Bauer C, Sant T, Manning L, Jones M, Rogers B, McCorkle D and Ferrell T L 2003 *Appl. Phys. Lett.* **83** 3428
- [19] Filhol F, Defay E, Divoux C, Zinck C and Delaye M T 2005 *Sensors Actuators A* **123-124** 483–9
- [20] Singh R, Kumar M and Chandra S 2005 *J. Mater. Sci.* **42** 4675–83
- [21] Dubois M A and Mural P 1999 *Appl. Phys. Lett.* **74** 3032–4
- [22] Pijolat M et al 2009 *Appl. Phys. Lett.* **95** 182106
- [23] Aissi M, Tourmier E, Dubois M A, Billard C, Ziad H and Plana R 2006 *IEEE Radio Frequency Integrated Circuit (RFIC) Symp.* (San Francisco, CA: Freeman) pp 37–40
- [24] Martin F, Mural P, Dubois M A and Pezous A 2004 *J. Vac. Sci. Technol. A* **22** 361
- [25] Sinha N, Wabiszewski G E, Mahameed R, Flemetsger V V, Tanner S M, Carpick R W and Piazza G 2009 *Appl. Phys. Lett.* **95** 053106
- [26] Karabalin R B, Matheny M H, Feng X L, Defay E, Le Rhun G, Marcoux C, Hentz S, Andreucci P and Roukes M L 2009 *Appl. Phys. Lett.* **95** 103111
- [27] Masel R I 1996 *Principles of Adsorption and Reaction on Solid Surfaces* (Hoboken, NJ: Wiley Interscience) p 240
- [28] Robins W P 1982 *Phase Noise in Signal Sources* (London: Peter Peregrinus)
- [29] Ekinci K L, Yang Y T and Roukes M L 2004 *J. Appl. Phys.* **95** 2682
- [30] Timoshenko S 1925 *J. Opt. Soc. Am.* **11** 233–55
- [31] Smits J G 1994 *IEEE/ASME J. MEMS* **3** 105–12
- [32] Brissaud M 2004 *J. Micromech. Microeng.* **14** 1507
- [33] Mahmoodi S N, Jalili N and Daqaq M F 2008 *IEEE Trans. Mechatro. (Atlanta, GA)* **13** 58
- [34] Ugural A C and Fenster S K 1995 *Advanced Strength and Applied Elasticity* (Saddle River, NJ: Prentice Hall) p 209
- [35] Adams J D, Manning L, Rogers B, Jones M and Minne S C 2005 *Sensors Actuators A* **121** 262–6
- [36] Ferrari V, Marioli D and Taroni A 2001 *IEEE Trans. Instrum. Meas.* **50** 1119–22
- [37] Signal Recovery Model 5184 Preamplifier, <http://www.signalrecovery.com/datasheets/5184PreampV7Web.pdf>
- [38] Bianco S et al 2006 *J. Vac. Sci. Technol. B* **24** 1803–9
- [39] Dubois M A and Mural P 2001 *J. Appl. Phys.* **89** 6389–95
- [40] Mishin S, Marx D R, Sylvia B, Lughi V, Turner K L and Clarke D R 2003 *IEEE Int. Ultrason. Symp. (Honolulu, HI)* **2** pp 2028–32
- [41] Iborra E, Olivares J, Clement M, Vergara L, Sanz-Hervas A and Sangrador J 2004 *Sensors Actuators A* **115** 501–7
- [42] Defay E, Zinck C, Malhaire C, Baboux N and Barbier D 2006 *Rev. Sci. Instrum.* **77** 103903
- [43] Rubiola E 1995 *Phase Noise and Frequency Stability in Oscillators* (Cambridge: Cambridge University Press)
- [44] Kharrat C, Colinet E and Voda A 2008 *IEEE Sensors* **1135**–8
- [45] Mile E, Jourdan G, Bargatin I, Labarthe S, Marcoux C, Andreucci P, Hentz S, Kharrat C, Colinet E and Duraffourg L 2010 *Nanotechnology* **21** 165504
- [46] Rinaldi M, Duick B, Zuniga C, Zuo C and Piazza G 2010 *IEEE Int. Conf. on Micro Elec. Mech. Syst. (MEMS 2010)* pp 132–5